

# Coordination Pore-Space Engineering in Robust Cage-Like Metal-Organic Frameworks for Highly Efficient CO<sub>2</sub> Capture from Flue Gas

Ziyu He, Jianjun You, Lei Zhang,\* Yang-Yang Xiong, Cheng-Xia Chen,\* Houan Zhang, Qianting Wang, Abdullah M. Al-Enizi, Ayman Nafady, and Shengqian Ma\*

Developing novel porous adsorbents for highly selective CO<sub>2</sub> from wet-hot flue gas represents one of the most promising technologies to mitigate the negative impact on the environment via suppressing CO<sub>2</sub> emissions, albeit it remains highly challenging due to the difficulty of achieving the trade-off among adsorption capacity, selectivity, adsorption enthalpy, and stability. Herein, a facile coordination pore-space engineering (CPSE) strategy is demonstrated to optimize the pore nanospace of the prototypical cage-like MOF, *proto*-MFOF-1, by virtue of an isostructural contraction protocol, for highly efficient CO<sub>2</sub> capture from wet-hot flue gas. Significantly, FJUT-1, with excellent physiochemical stability, presents significantly improved CO<sub>2</sub> capture capacity and CO<sub>2</sub>/N<sub>2</sub> selectivity compared with *proto*-MFOF-1, due to the contracted cage window size, preserved cage volume, and functionalized cage surface decorated with fluoride/sulfate (F<sup>-</sup>/SO<sub>4</sub><sup>2-</sup>) anions, and pyridine/benzene rings. Additionally, the practical separation performance for FJUT-1 is examined by transient breakthrough experiments at 298–343 K, demonstrating impressive CO<sub>2</sub> capture capacities of 2.29–0.80 mmol g<sup>-1</sup>, which can be reserved under high humidity. The distinct adsorption mechanism has been well disentangled by in situ SCXRD, in situ FTIR spectrum, and molecular modeling, in which the strong electrostatic O⋯C=O, multiple C-H⋯O hydrogen bonds, and guest-guest interactions, collaboratively result in the highly selective CO<sub>2</sub> capture performance.

## 1. Introduction

The climate change caused by excessive CO<sub>2</sub> emissions to the atmosphere, stemming from the combustion of fossil fuels, has incurred a series of global environmental concerns, including sea-level rise disasters, increases in extreme climate events, anabatic ecosystem damage, intensified droughts, etc., which pose a serious risk to human survival.<sup>[1,2]</sup> Seeking technologies that can effectively capture and store CO<sub>2</sub> from industry exhaust gases emitted from coal-fired power plants or carbon-intensive industries is necessary for reducing carbon emissions in the short term, owing to the domination of the traditional fossil fuel in the current energy framework. Therefore, the aqueous liquid-amine scrubbers' method, through a combination of physical and chemical adsorption mechanisms with CO<sub>2</sub> has been recognized as one of the most applicable and mature carbon capture technology.<sup>[3,4]</sup> However, it usually suffers from critical limitations involving high regeneration energies, reduced performance

L. Zhang, H. Zhang, Q. Wang  
School of Materials Science and Engineering  
Xiamen University of Technology  
Xiamen 361024, China  
E-mail: leizhang@xmut.edu.cn

Y.-Y. Xiong, C.-X. Chen  
GBRCE for Functional Molecular Engineering  
Lehn Institute of Functional Materials, IGCM  
School of Chemistry  
Sun Yat-Sen University  
Guangzhou 510006, China  
E-mail: chenx29@mail.sysu.edu.cn

S. Ma  
Department of Chemistry  
University of North Texas  
Denton, Texas 76201, USA  
E-mail: Shengqian.Ma@unt.edu

Z. He, J. You, L. Zhang, Q. Wang  
College of Materials Science and Engineering  
Fujian University of Technology  
Fuzhou 350118, China

A. M. Al-Enizi, A. Nafady  
Department of Chemistry  
College of Science  
King Saud University  
Riyadh 11451, Saudi Arabia



The ORCID identification number(s) for the author(s) of this article can be found under <https://doi.org/10.1002/adfm.202524748>

DOI: 10.1002/adfm.202524748

over time, increased costs, and equipment corrosion, due to the harsh implementation conditions. Therefore, it is necessary to develop novel CO<sub>2</sub> capture technologies with the nature of cost-/energy-efficiency to address these concerns.

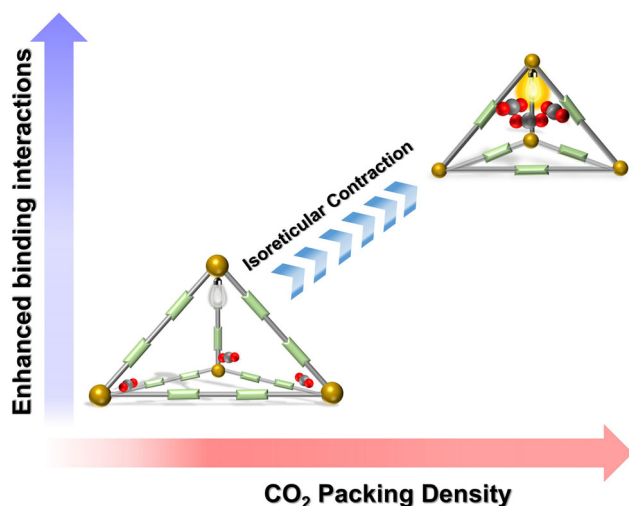
Recently, the nonthermal-driven adsorption approach based on porous solids has emerged as a favorable technology for CO<sub>2</sub> capture, attributed to its cost-/energy-efficiency and facile recyclability.<sup>[5,6]</sup> Thanks to their structural diversity and function tunability, metal-organic frameworks (MOFs), made of inorganic metal ions (clusters) and organic linkers via coordination bonds, have gained substantial attention in carbon capture.<sup>[7–11]</sup> The pore system of MOFs involving pore size, volume, shape, and surface environment can be finely tuned by virtue of the isostructural principle or reticular chemistry strategy, which in turn confers MOFs with great potential for capturing and sequestering CO<sub>2</sub> efficiently. However, concerning the realistic post-combustion CO<sub>2</sub> capture process from flue gas, the present competitive N<sub>2</sub> and moisture adsorption against CO<sub>2</sub>, together with the limited physicochemical stability of MOFs toward the acidic components (SO<sub>2</sub>/NO<sub>x</sub>) of wet-hot flue gas, impose a huge challenge for achieving highly selective and sustainable CO<sub>2</sub> capture. It has been proven that introducing some specific functionalities, such as open metal sites (OMSs), polar functional groups, or multiple-hydrogen sites, into MOFs can effectively promote selective CO<sub>2</sub> adsorption.<sup>[12–15]</sup> MOFs with OMSs are capable of achieving high CO<sub>2</sub> capture capacity through forming dative bonds with the oxygen of CO<sub>2</sub> but can be easily poisoned by the omnipresent moisture, leading to greatly reduced CO<sub>2</sub> uptakes, or even the collapse of frameworks.<sup>[16]</sup> Construction of nitrogen-adorned polar pore environments through incorporating aryl/alkyl amine moieties into MOFs can contribute to high selectivity for CO<sub>2</sub>, however, the amino groups also present high affinity toward other polarizable gases, especially for water molecules, which bind to amine groups too tightly to be replaced by CO<sub>2</sub>.<sup>[17]</sup> The similar competitive moisture adsorption phenomena can even be found in some moisture-stable MOFs.<sup>[18–21]</sup> For instance, the fluorinated MOF, NbOFFIVE-1-Ni, presents high uptake for trace CO<sub>2</sub> but a dramatically decreased CO<sub>2</sub> capture capacity under 74% humidity.<sup>[22]</sup> Therefore, the elaborate design of robust MOFs with highly CO<sub>2</sub> adsorption selectivity versus N<sub>2</sub> and moisture is highly desirable.

The construction of a hydrogen-rich pore in ultra-microporous MOFs holds great potential for selective CO<sub>2</sub> capture via multiple hydrogen-bonding interactions.<sup>[23–25]</sup> For instance, Fairen-Jimenez and coworkers described a flexibility-frustrating ultra-microporous MOF, CU-4, featuring a hydrogen-rich environment in the confined pore, which displayed high CO<sub>2</sub> selectivity in the presence of N<sub>2</sub> and water due to the reinforced confinement effect from strong multiple hydrogen bonds (HBs).<sup>[26]</sup> Moreover, the ultra-microporous nature may endow the frameworks with the possibility to form guest-guest interactions within the pores, further enhancing the molecular recognition for specific gas.<sup>[27–29]</sup> However, the enhanced recognition selectivity in this type of MOFs usually comes at the expense of capture capacity, resulting in a trade-off between selectivity and capture capacity.<sup>[30–32]</sup> In this respect, the design of cage-like robust MOFs, featuring large pore volume, small cavity window size, as well as functionalized pore surface, may provide an alternative

solution to address these concerns.<sup>[33–35]</sup> The small cavity window size and functionalized cage surface can confer the frameworks with high selectivity toward specific gases, while the large volume guarantees high gas uptakes, thus beneficial for balancing the trade-off between selectivity and capture capacity. For instance, the Zhang group developed a series of anion-pillared fluorinated cage-like MOFs, TIFSIX-Cu-TPA, SIFSIX-Cu-TPA, GeFSIX-Cu-TPA, and NbOFFIVE-Cu-TPA, with customized two types of interconnected cages, for highly efficient CO<sub>2</sub> capture from flue gas.<sup>[36]</sup> Thereinto, the resultant TIFSIX-Cu-TPA showcased high CO<sub>2</sub> adsorption capacity, high IAST selectivity, and good chemical stability toward acids, due to the small cage window size, large pore volume, and fluorine functionalized pore surface. The Feng and Bu groups developed a pore space partition strategy to construct a variety of cage-like mixed-ligand MOFs (PSP-MOFs) for gas adsorption and separation.<sup>[37–39]</sup> The high connectivity of M<sub>3</sub>O clusters endowed the frameworks with high physicochemical stability. The introduction of the second spacer relocated the primitive pore system, specifically compartmentalizing the channels into small cages with a small window size, functionalized cage surface, and appropriate cage volume, thus enabling the MOFs to efficiently capture CO<sub>2</sub>. Nevertheless, the simultaneous implementation of high CO<sub>2</sub> capture capacity, high selectivity, low regeneration energy, and high physicochemical stability in cage-like MOFs remains a daunting challenge, probably due to the lack of a feasible strategy to finely engineer the coordination pore-space of cage-based MOFs.

Recently, we developed an isorecticular contraction (IRC) approach to construct fluoride- and sulfate-bridging Co<sub>4</sub>-cluster-based cage-like MOFs, by immobilizing shorter tripodal organic carboxylic acid and pyridine linkers, and inorganic fluoride (F<sup>-</sup>) and sulfate (SO<sub>4</sub><sup>2-</sup>)-bridging Co<sub>4</sub> clusters into the defined position of the prototypical MOF matrix.<sup>[40]</sup> This approach can finely regulate the cage system involving cage window size, volume, shape, and surface, thus opening up a new way for realizing cage-like MOFs with optimized pore-space for gas adsorption and separation, such as C<sub>2</sub>H<sub>2</sub>/CO<sub>2</sub> and C<sub>2</sub>H<sub>2</sub>/C<sub>2</sub>H<sub>4</sub> separation. Nevertheless, it hasn't been utilized to achieve selective CO<sub>2</sub> capture from wet-hot flue gas. Considering that the pyridine moieties and F<sup>-</sup>/SO<sub>4</sub><sup>2-</sup> anions can serve as potential CO<sub>2</sub> binding sites, we hypothesize that the introduction of pyridine moieties and F<sup>-</sup>/SO<sub>4</sub><sup>2-</sup> anions into the appropriate cage space may result in significantly improved selectivity for capturing CO<sub>2</sub>. More importantly, immobilizing highly connected Co<sub>4</sub> clusters into cage-like MOFs with a small cage window size, via strong Co–O/N bonds, may enable the resultant MOFs with greatly enhanced physicochemical stability, especially under wet-hot conditions.

Bearing these in mind, we describe a facile coordination pore-space engineering (CPSE) strategy to optimize the pore system via implementing IRC protocol for post-combustion CO<sub>2</sub> capture (**Scheme 1**). By substituting the longer 4,4',4''-benzene-1,3,5-triyl-tribenzoate (BTB), 2,4,6-tri(4-pyridinyl)-1,3,5-triazine (TPT) linkers of the prototypical MFOF-1 (*proto*-MFOF-1) with shorter 4,4',4''-nitrilotribenzoic acid (NTB), and tri(pyridin-4-yl)amine (TPA), FJUT-1 was afforded. This MOF is functionalized with fluoride/sulfate anions, as well as pyridine moieties, and features an optimal pore system for selective CO<sub>2</sub> capture.



**Scheme 1.** Schematic illustration of coordination pore-space engineering (CPSE) strategy for enhancing CO<sub>2</sub> binding interactions in the confined cage nano-space.

Compared with *proto*-MFOF-1, FJUT-1 displays much higher CO<sub>2</sub> uptake (4.97 mmol g<sup>-1</sup> at 298 K and 1 bar) along with higher CO<sub>2</sub>/N<sub>2</sub> selectivity (54.88 at 298 K and 1 bar), and modest adsorption enthalpy (35.85 kJ mol<sup>-1</sup>) for facile regeneration attributed to the reduced cage window size, appropriate cage volume, and the functionalized cage surface. Moreover, FJUT-1 with the nature of easy scale-up synthesis (12 g scale) presents exceptional chemical stability in harsh acidic and basic aqueous solutions (pH = 1–13, at 100 °C) due to the highly connected Co<sub>4</sub>-clusters and strong Co-O/N coordination bonds, thus endowing the MOF with the ability for practical CO<sub>2</sub> capture from wet-hot flue gas. Remarkably, FJUT-1 exhibits highly selective separation performance at 298–343 K, whether under dry or humid (80%) conditions, with the CO<sub>2</sub> capture capacity of 2.18–0.80 mmol g<sup>-1</sup> as evidenced by dynamic breakthrough experiments. The underlying selective adsorption mechanism has been well deciphered through in situ FT-IR, in situ SCXRD, and molecular simulations, wherein the electrostatic O<sub>(SO<sub>4</sub><sup>2-</sup>)...C=O and multiple C–H<sub>(pyridine)</sub>...O=C interactions within the cages synergistically lead to the highly selective CO<sub>2</sub> capture performance.</sub>

## 2. Results and Discussion

### 2.1. Design Cage-Like Mixed-Ligand MOF with Optimized Pore-Nanospace via CPSE Strategy

To manifest the feasibility of the CPSE strategy for optimizing the pore nanospace of cage-like MOFs, the prototypical MFOF-1 (*proto*-MFOF-1) was prepared through the solvothermal reaction of BTB, TPT, and CoSO<sub>4</sub> in a mixed *N*, *N*-dimethylacetamide/methanol/1,4-dioxane (DMA/MeOH/Diox) solution (Figure 1).<sup>[41]</sup> The *proto*-MFOF-1 features three distinct cages, one octahedral cage (O<sub>c</sub>) and two tetrahedral cages (T<sub>c</sub>-A and T<sub>c</sub>-B), adorned with fluoride (F<sup>-</sup>) anions, sulfate (SO<sub>4</sub><sup>2-</sup>) anions, and pyridine/benzene groups, which can be regulated via replacing the original tripodal linkers in *proto*-MFOF-1. As shown in Figure 1, the replacement of BTB and

TPT linkers with contracted NTB and TPA linkers produced the isostructural FJUT-1, possessing similar cage structures yet optimized pore size/volume/surface, via solvothermal reactions in DMA/CH<sub>3</sub>OH/Diox mixture (2:2:1, v:v:v).<sup>[40]</sup> Note that the introduction of contracted organic linkers leads to reduced cage size, in which the cage cavity diameters in FJUT-1 decrease from 10.6 to 7.6 Å for cage O<sub>c</sub>, 11.0 to 8.4 Å for cage T<sub>c</sub>-A, and 7.0 to 5.2 Å for T<sub>c</sub>-B, respectively, corresponding to the cage window size reducing from 7.5 to 5.4 Å for cage O<sub>c</sub>, 7.0 to 5.0 Å for cage T<sub>c</sub>-A, and 6.2 to 4.5 Å for T<sub>c</sub>-B, in comparison with *proto*-MFOF-1. The reduced cage window size, combined with the functionalized cage surface endows FJUT-1 with enhanced selectivity, while the preserved suitable cage volume bestows the framework with improved gas capture capacity due to the consolidated cage confinement effect in FJUT-1, holding the potential for achieving highly selective CO<sub>2</sub> capture. Additionally, compared with *proto*-MFOF-1, the decorated F<sup>-</sup>, SO<sub>4</sub><sup>2-</sup>, and pyridines/benzenes moieties in the contractive cages of FJUT-1 provide multiple yet reinforced action sites for CO<sub>2</sub>, thus further promoting the selective adsorption of CO<sub>2</sub> via O...C=O and multiple C–H...O=C interactions.

### 2.2. Characterizations of Cage-Like Mixed-Ligand MOFs

Before assessing the CO<sub>2</sub> capture performance, the synthesized cage-like MOFs were characterized by scanning electron microscopy (SEM), powder X-ray diffraction (PXRD) patterns, thermogravimetric analysis (TGA), and N<sub>2</sub> adsorption at 77 K (Figures S2–S12, Supporting Information). Specifically, SEM images revealed the octahedral morphology of FJUT-1 (Figure S2, Supporting Information). PXRD patterns were conducted to verify the phase purity of *proto*-MFOF-1 and FJUT-1 (Figures S5 and S8, Supporting Information). The chemical stability of *proto*-MFOF-1 and FJUT-1 was evaluated by immersing the samples in boiling aqueous solution with different pH values (pH = 1–13) for a certain time. PXRD patterns showed that FJUT-1 still retained structural integrity and high crystallinity, which was further confirmed by SEM images, CO<sub>2</sub>/N<sub>2</sub> adsorption isotherms, suggesting its excellent chemical stability under harsh acidic and basic conditions, thus presenting great potential for practical CO<sub>2</sub> capture from wet-hot flue gas containing corrosive gases (Figure 2d; Figures S4, S7, S12, S15 and S16, Supporting Information). On the contrary, *proto*-MFOF-1 lost its crystallinity after being treated boiling aqueous solution with pH values of 1 and 13 (Figures S3 and S6, Supporting Information). TGA curve was measured to reveal that FJUT-1 can be stable up to 380 °C (Figure S9, Supporting Information). N<sub>2</sub> adsorption isotherms at 77 K were performed to assess the porosity of *proto*-MFOF-1 and FJUT-1, revealing the saturated adsorption of 578.29 and 307.98 cm<sup>3</sup> g<sup>-1</sup>, respectively (Figure S10, Supporting Information). Compared with the *proto*-MFOF-1 (2214 m<sup>2</sup> g<sup>-1</sup>, 0.90 cm<sup>3</sup> g<sup>-1</sup>), the BET surface area and pore volume of FJUT-1 reduce to 1199 m<sup>2</sup> g<sup>-1</sup> and 0.47 cm<sup>3</sup> g<sup>-1</sup> as a result of the contracted cage cavity of FJUT-1 (Table S3, Supporting Information). The density functional theory (DFT) method was used to examine the pore size distributions of *proto*-MFOF-1 and FJUT-1, disclosing that the pore sizes of FJUT-1 decrease to 5.6 and 6.9 Å compared with the *proto*-MFOF-1 (6.8 and 10.1 Å), indicating the enhanced cage

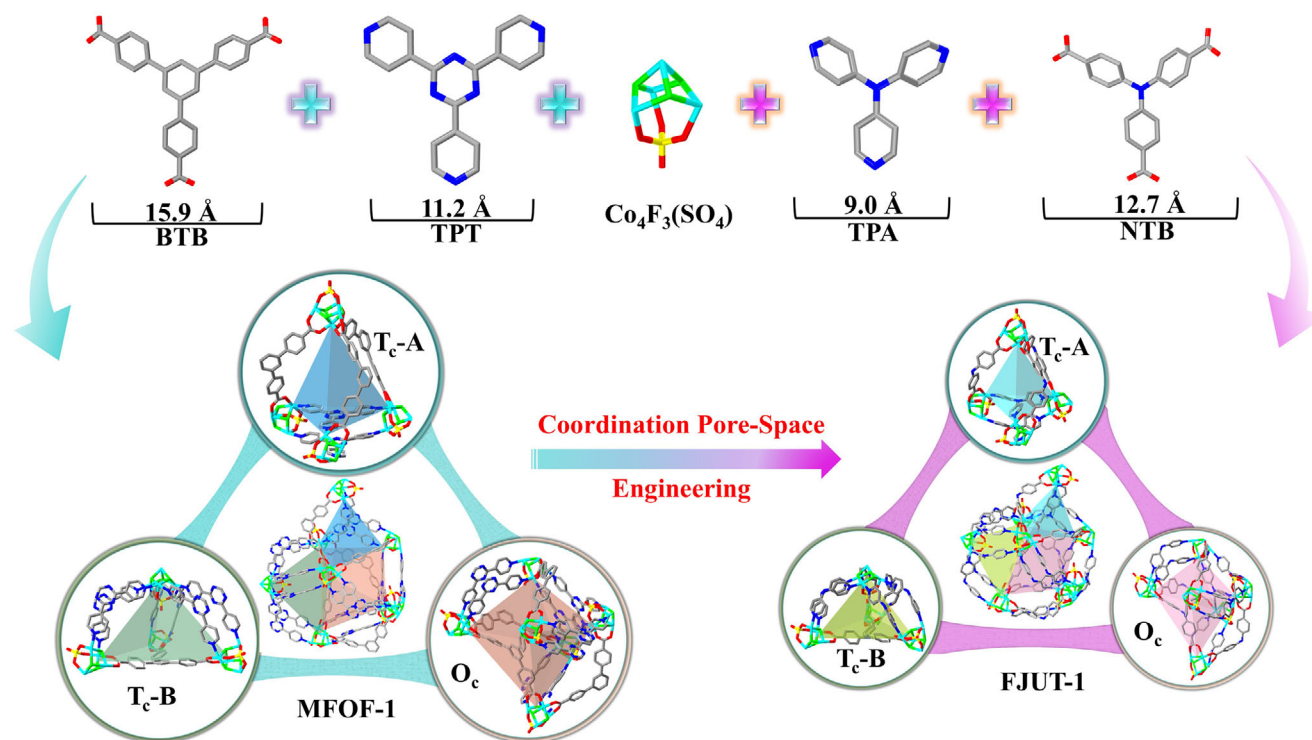


**Figure 1.** Schematic illustration of three major cages with different sizes in *proto*-MFOF-1 and FJUT-1. Atom color codes: Co, turquoise; C, gray; N, blue; O, red; F, bright green; S, yellow. H atoms are omitted for clarity.

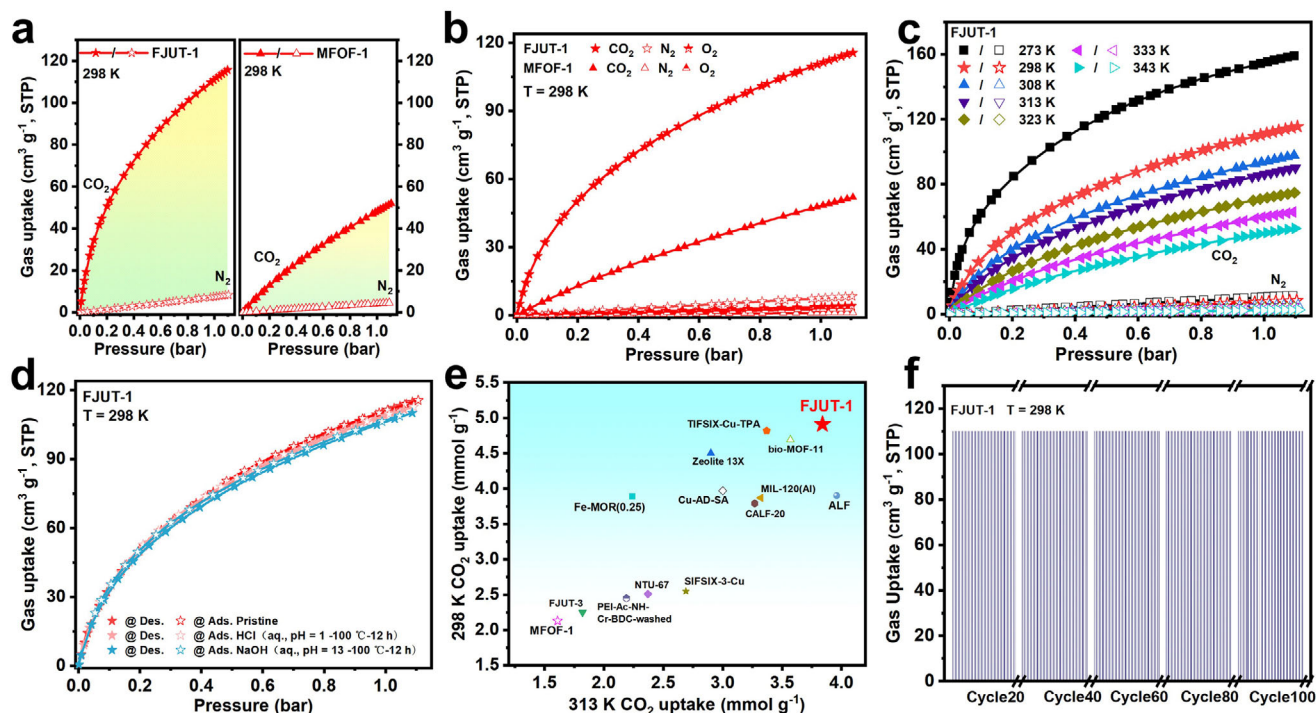


**Figure 2.** Gas adsorption properties of *proto*-MFOF-1 and FJUT-1. a)  $\text{CO}_2$  and  $\text{N}_2$  adsorption isotherms of MFOF-1 and FJUT-1 at 298 K. b)  $\text{CO}_2$ ,  $\text{N}_2$ , and  $\text{O}_2$  adsorption isotherms of MFOF-1 and FJUT-1 at 298 K. c)  $\text{CO}_2$  and  $\text{N}_2$  adsorption isotherms of FJUT-1 under various temperatures. d)  $\text{CO}_2$  adsorption isotherms at 298 K for FJUT-1 after treatment with different conditions. e) Comparison of the  $\text{CO}_2$  uptake at 298 K and 313 K for FJUT-1 with the best-performing MOF materials. f) One hundred times consecutive adsorption cycles of  $\text{CO}_2$  gas for FJUT-1 at 298 K.

confinement effect in FJUT-1, beneficial for improving CO<sub>2</sub> adsorptive selectivity (Figure S10 and Table S3, Supporting Information). Note that while the pore volume of FJUT-1 reduces to some extent compared with the *proto*-MFOF-1, the remained pore volume combined with the reduced pore size is more conducive to achieving the trade-off between high CO<sub>2</sub> uptake and high CO<sub>2</sub> selectivity. Moreover, the lack of OMSs in FJUT-1 confers the adsorbents with facile regeneration ability, lowering the energy requirements. Given that the large-scale synthesis is another critical metric in the realistic industrial separation process, the scale-up synthesis experiments were performed to evaluate the feasibility of producing FJUT-1 in a gram scale. The results unveiled that FJUT-1 can be afforded on a 12 g scale, which presents high crystallinity, chemical stability, and CO<sub>2</sub> capture capacity (Figures S1, S7 and S14, Supporting Information), compared with FJUT-1 samples produced on a small scale (75 mg scale), thus confirming the technical feasibility of large-scale synthesis.

### 2.3. Single-Component Adsorption Isotherms

To examine the gas separation performance, CO<sub>2</sub> and N<sub>2</sub> adsorption isotherms were carried out at 273–343 K. As illustrated in Figure 2a,b, both MOFs display much higher CO<sub>2</sub> uptakes (47.65 cm<sup>3</sup> g<sup>-1</sup>, 2.13 mmol g<sup>-1</sup> for MFOF-1; 111.33 cm<sup>3</sup> g<sup>-1</sup>, 4.97 mmol g<sup>-1</sup> for FJUT-1) than N<sub>2</sub> (4.15 cm<sup>3</sup> g<sup>-1</sup>, 0.19 mmol g<sup>-1</sup> for MFOF-1; 7.42 cm<sup>3</sup> g<sup>-1</sup>, 0.33 mmol g<sup>-1</sup> for FJUT-1), and O<sub>2</sub> (2.64 cm<sup>3</sup> g<sup>-1</sup>, 0.12 mmol g<sup>-1</sup> for MFOF-1; 3.63 cm<sup>3</sup> g<sup>-1</sup>, 0.16 mmol g<sup>-1</sup> for FJUT-1) at 298 K and 1 bar, suggesting good CO<sub>2</sub>/N<sub>2</sub> separation potential. Additionally, FJUT-1 has a much higher CO<sub>2</sub> adsorption capacity than *proto*-MFOF-1, particularly at 298 K and 0.15 bar (Table S3, Supporting Information). Its CO<sub>2</sub> uptake for FJUT-1 (44.03 cm<sup>3</sup> g<sup>-1</sup>, 1.96 mmol g<sup>-1</sup>) is more than four times that of MFOF-1 (10.45 cm<sup>3</sup> g<sup>-1</sup>, 0.46 mmol g<sup>-1</sup>). This enhancement stems from FJUT-1's contracted cage window size and appropriate cage volume, which boost CO<sub>2</sub> capture from flue gas. Noteworthy, the CO<sub>2</sub> uptake for FJUT-1 at 298 K and 1 bar is higher than many top-performing MOFs, such as SIFSIX-Cu-TPA (107.9 cm<sup>3</sup> g<sup>-1</sup>, 4.82 mmol g<sup>-1</sup>),<sup>[36]</sup> TISIX-Cu-TPA (105.4 cm<sup>3</sup> g<sup>-1</sup>, 4.71 mmol g<sup>-1</sup>),<sup>[36]</sup> Zeolite 13X (100.8 cm<sup>3</sup> g<sup>-1</sup>, 4.50 mmol g<sup>-1</sup>),<sup>[42]</sup> dptz-CuTiF<sub>6</sub> (90.49 cm<sup>3</sup> g<sup>-1</sup>, 4.04 mmol g<sup>-1</sup>),<sup>[43]</sup> Fe-MOR (0.25) (87.14 cm<sup>3</sup> g<sup>-1</sup>, 3.89 mmol g<sup>-1</sup>),<sup>[44]</sup> ALF (89.15 cm<sup>3</sup> g<sup>-1</sup>, 3.98 mmol g<sup>-1</sup>),<sup>[23]</sup> CALF-20 (84.89 cm<sup>3</sup> g<sup>-1</sup>, 3.79 mmol g<sup>-1</sup>),<sup>[45]</sup> LIFM-26(Fe[II]/Fe[III]) (80 cm<sup>3</sup> g<sup>-1</sup>, 3.57 mmol g<sup>-1</sup>),<sup>[46]</sup> NTU-67 (56.22 cm<sup>3</sup> g<sup>-1</sup>, 2.51 mmol g<sup>-1</sup>),<sup>[47]</sup> CALF-20M-w (52.86 cm<sup>3</sup> g<sup>-1</sup>, 2.36 mmol g<sup>-1</sup>),<sup>[48]</sup> but lower than UiO-66-(OH)<sub>2</sub> (126.11 cm<sup>3</sup> g<sup>-1</sup>, 5.63 mmol g<sup>-1</sup>)<sup>[49]</sup> with pores decorated with Lewis basic hydroxy groups, and Mg-MOF-74 (163.07 cm<sup>3</sup> g<sup>-1</sup>, 7.28 mmol g<sup>-1</sup>)<sup>[44]</sup> with pores adorned with OMSs (Figure 2e; Table S6, Supporting Information). Considering that the post-combustion capture of CO<sub>2</sub> from flue gas is usually implemented at high temperature, the CO<sub>2</sub> adsorption isotherms were collected at 313–343 K, disclosing a gradually decreased trend from 86.09 to 49.54 cm<sup>3</sup> g<sup>-1</sup> (Figure 2c, Figures S17–S19, Supporting Information). As depicted in Table S3 (Supporting Information), the CO<sub>2</sub> uptakes for FJUT-1 are 86.09 cm<sup>3</sup> g<sup>-1</sup> (3.84 mmol g<sup>-1</sup>), 70.85 cm<sup>3</sup> g<sup>-1</sup> (3.16 mmol g<sup>-1</sup>), 59.72 cm<sup>3</sup> g<sup>-1</sup> (2.67 mmol g<sup>-1</sup>), and 49.54 cm<sup>3</sup> g<sup>-1</sup> (2.21 mmol g<sup>-1</sup>) at 313, 323, 333, and 343 K, and 1 bar, respectively, implying a good adap-

tiveness to flue gas conditions at different temperatures. The CO<sub>2</sub> adsorption capacity for FJUT-1 at 313–343 K also is much higher than those of *proto*-MFOF-1 (36.05 cm<sup>3</sup> g<sup>-1</sup>, 1.61 mmol g<sup>-1</sup> at 313 K and 1 bar, 29.28 cm<sup>3</sup> g<sup>-1</sup>, 1.31 mmol g<sup>-1</sup> at 323 K and 1 bar, 23.28 cm<sup>3</sup> g<sup>-1</sup>, 1.04 mmol g<sup>-1</sup> at 333 K and 1 bar, and 18.88 cm<sup>3</sup> g<sup>-1</sup>, 0.84 mmol g<sup>-1</sup> at 343 K and 1 bar), further validating the efficiency of CPSE strategy for improving CO<sub>2</sub> selective adsorption performance via finely regulating the pore nanospace of cage-like MOFs (Figure S13, Supporting Information). In addition, consecutive adsorption isotherms were measured to disclose the excellent recyclability of FJUT-1, in which FJUT-1 can be used at least one hundred times continuously without any loss of adsorption performance (Figure 2f). Note that the CO<sub>2</sub> uptake for FJUT-1 at 313 K and 1 bar is higher than many benchmark adsorbents, such as bio-MOF-11 (79.97 cm<sup>3</sup> g<sup>-1</sup>, 3.57 mmol g<sup>-1</sup>),<sup>[50]</sup> SIFSIX-Cu-TPA (75.49 cm<sup>3</sup> g<sup>-1</sup>, 3.37 mmol g<sup>-1</sup>),<sup>[36]</sup> MIL-120(Al) (74.37 cm<sup>3</sup> g<sup>-1</sup>, 3.32 mmol g<sup>-1</sup>),<sup>[30]</sup> CALF-20 (73.25 cm<sup>3</sup> g<sup>-1</sup>, 3.27 mmol g<sup>-1</sup>),<sup>[48]</sup> and TIFSIX-Cu-TPA (69.66 cm<sup>3</sup> g<sup>-1</sup>, 3.11 mmol g<sup>-1</sup>)<sup>[36]</sup> (Figure 2e). To examine the CO<sub>2</sub>/N<sub>2</sub> separation potential, the CO<sub>2</sub>/N<sub>2</sub> and CO<sub>2</sub>/O<sub>2</sub> selectivities on *proto*-MFOF-1 and FJUT-1 were calculated by ideal adsorbed solution theory (IAST) (Figures S23–S26 and S30–S35, Supporting Information). The IAST CO<sub>2</sub>/N<sub>2</sub> (15:85, v:v) and CO<sub>2</sub>/O<sub>2</sub> (75:25, v:v) selectivities for FJUT-1 are 54.88 and 6138.96 at 298 K and 1 bar, much higher than those of *proto*-MFOF-1 (16.66 and 28.44), suggesting improved separation performance as a consequence of the enhanced confinement effect in FJUT-1. Overall, these results show that the CPSE strategy endows FJUT-1 with optimized pore nanospace involving reduced cage window size, appropriate cage volume, as well as functionalized cage surface adorned with F<sup>-</sup>/SO<sub>4</sub><sup>2-</sup> anions and pyridine/benzene rings, which collaboratively contribute to the enhanced CO<sub>2</sub>/N<sub>2</sub> and CO<sub>2</sub>/O<sub>2</sub> separation performance.

Since the adsorption enthalpy (Q<sub>st</sub>) is another crucial metric for evaluating the affinity toward gases and the regenerated energy requirement, the CO<sub>2</sub> and N<sub>2</sub> Q<sub>st</sub> for *proto*-MFOF-1 and FJUT-1 were calculated using the Clausius-Clapeyron equation based on the virial fitting parameters of CO<sub>2</sub> adsorption isotherms at 273, 298, and 313 K. As depicted in Figures S20 and S21 (Supporting Information), both MOFs show higher CO<sub>2</sub> Q<sub>st</sub> values than N<sub>2</sub> in the whole adsorption region, suggesting that they have a stronger affinity for CO<sub>2</sub>. In comparison with *proto*-MFOF-1 (23.15 kJ mol<sup>-1</sup>), FJUT-1 exhibits higher CO<sub>2</sub> Q<sub>st</sub> (35.85 kJ mol<sup>-1</sup>) at near-zero coverage, implying the stronger framework-CO<sub>2</sub> interactions in FJUT-1 ascribed to the reduced pore size. It is very important to highlight that the CO<sub>2</sub> Q<sub>st</sub> value for FJUT-1 is much lower than many adsorbents featuring -NH<sub>2</sub>/<sub>-OH</sub> groups, such as aqueous liquid-amine (105 kJ mol<sup>-1</sup>),<sup>[43]</sup> mmen-CuBTri (96 kJ mol<sup>-1</sup>),<sup>[51]</sup> een-MOF/Al-Si (73–75 kJ mol<sup>-1</sup>),<sup>[52]</sup> mmen-Mg<sub>2</sub>(dobpdc) (71 kJ mol<sup>-1</sup>),<sup>[53]</sup> CD-MOF-2 (67.2 kJ mol<sup>-1</sup>),<sup>[54,55]</sup> MOF-808-Gly (46 kJ mol<sup>-1</sup>),<sup>[56]</sup> and many MOFs carrying OMSs like Mg-MOF-74 (47 kJ mol<sup>-1</sup>),<sup>[57]</sup> NKMOF-1-Ni (40.9 kJ mol<sup>-1</sup>),<sup>[58]</sup> LIFM-26(Fe[II]/Fe[III]) (37.8 kJ mol<sup>-1</sup>),<sup>[46]</sup> and other MOFs like SIFSIX-3-Cu (54 kJ mol<sup>-1</sup>),<sup>[59]</sup> MIL-120(Al)-AP (41 kJ mol<sup>-1</sup>),<sup>[60]</sup> SIFSIX-3-Zn (45 kJ mol<sup>-1</sup>),<sup>[59]</sup> CALF-20M-w (41.9 kJ mol<sup>-1</sup>),<sup>[48]</sup> CALF-20 (36.8 kJ mol<sup>-1</sup>),<sup>[48]</sup> and NboFFIVE-Cu-TPA (37.76 kJ mol<sup>-1</sup>) (Table S6, Supporting Information),<sup>[36]</sup> implying the low regeneration energy requirement for post-combustion CO<sub>2</sub> capture from flue gas.

## 2.4. Breakthrough Experiments Studies

To evaluate the practical CO<sub>2</sub> separation potential of *proto*-MFOF-1 and FJUT-1, transient breakthrough experiments were carried out under dry or humid conditions at 298–343 K and 1 bar, wherein CO<sub>2</sub>/N<sub>2</sub> (15:85, v:v) gas mixture flowed over a fixed-bed filled with the samples of *proto*-MFOF-1 or FJUT-1 at a flow rate of 2, 5, or 10 mL min<sup>-1</sup> (Figure 3a–h, Figures S47–S60, Supporting Information). As represented in Figure 3, both MOFs are capable of achieving CO<sub>2</sub>/N<sub>2</sub> separation at all the different temperatures, including 298, 313, 323, 333, and 343 K, in which N<sub>2</sub> eluted out immediately while CO<sub>2</sub> remained in the column for a certain time. Moreover, FJUT-1 displays much longer breakthrough time than that of *proto*-MFOF-1, suggesting the superior CO<sub>2</sub>/N<sub>2</sub> separation performance for FJUT-1 (Figure 3a–c). Since the breakthrough time is an important parameter for evaluating the gas separation potential. For CO<sub>2</sub>/N<sub>2</sub> (15:85, v:v) gas mixture at a flow rate of 2 mL min<sup>-1</sup> (dry condition), the breakthrough intervals between CO<sub>2</sub> and N<sub>2</sub> for FJUT-1 were calculated as 119.24 min g<sup>-1</sup> (298 K), 85.16 min g<sup>-1</sup> (313 K), 64.67 min g<sup>-1</sup> (323 K), 49.66 min g<sup>-1</sup> (333 K), and 34.63 (343 K) min g<sup>-1</sup>. These correspond to CO<sub>2</sub> capture capacities of 2.18 mmol g<sup>-1</sup> (298 K), 1.68 mmol g<sup>-1</sup> (313 K), 1.26 mmol g<sup>-1</sup> (323 K), 1.03 mmol g<sup>-1</sup> (333 K), and 0.80 mmol g<sup>-1</sup> (343 K) (Figure S46, Supporting Information), respectively, which are comparable with many top-performing adsorbents, such as SIFSIX-Cu-TPA (2.30 mmol g<sup>-1</sup> for CO<sub>2</sub>/N<sub>2</sub> = 15:85, 5 mL min<sup>-1</sup>, 298 K, dry),<sup>[36]</sup> GeFSIX-Cu-TPA (2.20 mmol g<sup>-1</sup> for CO<sub>2</sub>/N<sub>2</sub> = 15:85, 5 mL min<sup>-1</sup>, 298 K, dry),<sup>[36]</sup> TIFSIX-Cu-TPA (2.10 mmol g<sup>-1</sup> for CO<sub>2</sub>/N<sub>2</sub> = 15:85, 5 mL min<sup>-1</sup>, 298 K, dry),<sup>[36]</sup> NbOFFIVE-Cu-TPA (1.80 mmol g<sup>-1</sup> for CO<sub>2</sub>/N<sub>2</sub> = 15:85, 5 mL min<sup>-1</sup>, 298 K, dry),<sup>[36]</sup> MIL-120 (1.22 mmol g<sup>-1</sup> for CO<sub>2</sub>/N<sub>2</sub> = 15:85, 2 mL min<sup>-1</sup>, 298 K, dry),<sup>[30]</sup> CU-4 (1.06 mmol g<sup>-1</sup> for CO<sub>2</sub>/N<sub>2</sub> = 10:90, 6.6 mL min<sup>-1</sup>, 293 K, dry).<sup>[26]</sup> Additionally, the CO<sub>2</sub> capture capacity for FJUT-1 was determined to be 2.43, 1.57, 1.07, and 0.78 mmol g<sup>-1</sup> based on the flow rates of 5 mL min<sup>-1</sup> at 298, 313, 333, and 343 K (Figure S55, Supporting Information).

To further examine the separation performance, wet (60 and 80%) mixed gas was introduced into the fixed-bed to imitate the practical condition of industrial flue gas at 298 and 343 K (Figures S53–S59, Supporting Information). Impressively, FJUT-1 shows comparable separation performance with those under dry conditions, even at 60% humidity. FJUT-1 presents improved CO<sub>2</sub>/N<sub>2</sub> separation potential, probably due to the co-adsorbed water molecules boost the adsorption of CO<sub>2</sub> (vide infra), thus demonstrating the excellent moisture tolerance of FJUT-1 (Figure S53, Supporting Information). The calculated breakthrough intervals between CO<sub>2</sub> and N<sub>2</sub> are 122.06 (60%) and 117.88 (80%) min g<sup>-1</sup> based on a single breakthrough curve with a flow rate of 2 mL min<sup>-1</sup> at 298 K and 1 bar, respectively, corresponding to the CO<sub>2</sub> capture capacity of 2.54 and 2.02 mmol g<sup>-1</sup>. In addition to this, FJUT-1 also exhibits good CO<sub>2</sub>/N<sub>2</sub> separation performance with a flow rate of 5 mL min<sup>-1</sup> under 80% humidity at 333 K and 1 bar, indicating the realistic post-combustion CO<sub>2</sub> capture potential from wet-hot flue gas (Figure S57, Supporting Information). The cycling breakthrough experiments were performed under dry and humid conditions at 298–343 K to assess the recyclability, which revealed that FJUT-1 presents only a negligible decrease in CO<sub>2</sub> capture capacity after five cycles, demonstrating its outstanding recyclability and durability, further confirmed

by the PXRD patterns (Figure 3e–h; Figures S8, S51, and S52, Supporting Information). It is worth noting that FJUT-1 presents an exceptionally high CO<sub>2</sub> capture capacity under high humidity (>70%) based on a single breakthrough curve, outperforming all the benchmark MOFs reported so far (Figure 3i). To evaluate the practical regeneration energy requirements, the breakthrough experiments were conducted under 80% humidity at 298 K with a flow rate of 10 mL min<sup>-1</sup>, in which the absorbent materials were regenerated through purging He flow with a rate of 10 mL min<sup>-1</sup> for 3 h at room temperature. For FJUT-1, almost the same breakthrough intervals were observed for at least five runs, and then gradually decreased to 15 min g<sup>-1</sup> after thirty cycles of breakthrough experiments (Figure S60, Supporting Information). In contrast, zeolite 13X showed a noticeable and continuous drop in CO<sub>2</sub> capture capacity after the first run with the same regeneration protocol (Figure S61, Supporting Information). It can be concluded that FJUT-1 can function as an effective adsorbent for practical post-combustion CO<sub>2</sub> capture from wet-hot flue gas.

To quantitatively evaluate the CO<sub>2</sub> capture potential of FJUT-1 from flue gas, six criteria are proposed to be carefully considered: high CO<sub>2</sub> uptake at 313 K and 1 bar (>3.60 mmol g<sup>-1</sup>), high CO<sub>2</sub>/N<sub>2</sub> selectivity at 313 K and 1 bar (>60), excellent physiochemical stability (thermal stability: > 550 K, chemical stability: stable in acidic and basic conditions with pH values ranging from 1 to 13 at 373 K), moderate CO<sub>2</sub> Q<sub>st</sub> (<40 kJ mol<sup>-1</sup>), good CO<sub>2</sub> capture capacity (>2 mmol g<sup>-1</sup>) based on breakthrough curve, good CO<sub>2</sub> capture capacity under 80% humidity (>2 mmol g<sup>-1</sup>) based on breakthrough curve (Table S7, Supporting Information). Specifically, FJUT-1 featuring moderate CO<sub>2</sub> Q<sub>st</sub> (35.85 kJ mol<sup>-1</sup>), exhibits high CO<sub>2</sub> uptake (3.84 mmol g<sup>-1</sup>) at 313 K and 1 bar, which is higher than many top-performing MOFs, such as bio-MOF-11 (3.57 mmol g<sup>-1</sup>),<sup>[50]</sup> SIFSIX-Cu-TPA (3.37 mmol g<sup>-1</sup>),<sup>[36]</sup> MIL-120(Al) (3.32 mmol g<sup>-1</sup>),<sup>[30]</sup> and CALF-20 (3.27 mmol g<sup>-1</sup>).<sup>[48]</sup> In addition, FJUT-1 displays good CO<sub>2</sub>/N<sub>2</sub> selectivity of 69.1 at 313 K and 1 bar (Figure S20, Supporting Information). Transient breakthrough experiments reveal that FJUT-1 features high CO<sub>2</sub> capture capacity (2.29 and 2.29 mmol g<sup>-1</sup> under dry and 80% humid conditions at 298 K with a flow rate of 10 mL min<sup>-1</sup>). Together with its excellent physiochemical stability (thermal stability: stable up to 653 K, chemical stability: stable in pH = 1–13 boiling aqueous solutions), and easy scale-up synthesis (12 g scale), FJUT-1 is adequate for achieving the six prerequisites, thus proving its great potential for post-combustion capture of CO<sub>2</sub> from wet-hot flue gas (Figure 2e; Figures S1, S7, S9, S17, and S54 and Table S8, Supporting Information). Note that FJUT-1 presents superior CO<sub>2</sub> capture potential from wet-hot flue gas than many benchmark MOF adsorbents (Figure 3j; Table S8, Supporting Information).

## 2.5. In Situ FT-IR Spectroscopy

The preferential CO<sub>2</sub> adsorption promoted the further investigation of the CO<sub>2</sub> fixation mechanism via in situ FT-IR spectroscopy (Figure 4). Initially, the samples of FJUT-1 were activated under high vacuum at 80 °C for 12 h to remove the trapped guest molecules in the cage cavity, and then cooled to room temperature to collect the IR spectra of *proto*-MFOF-1 and FJUT-1. As shown in Figure 4a, both spectra are dominated by characteristic

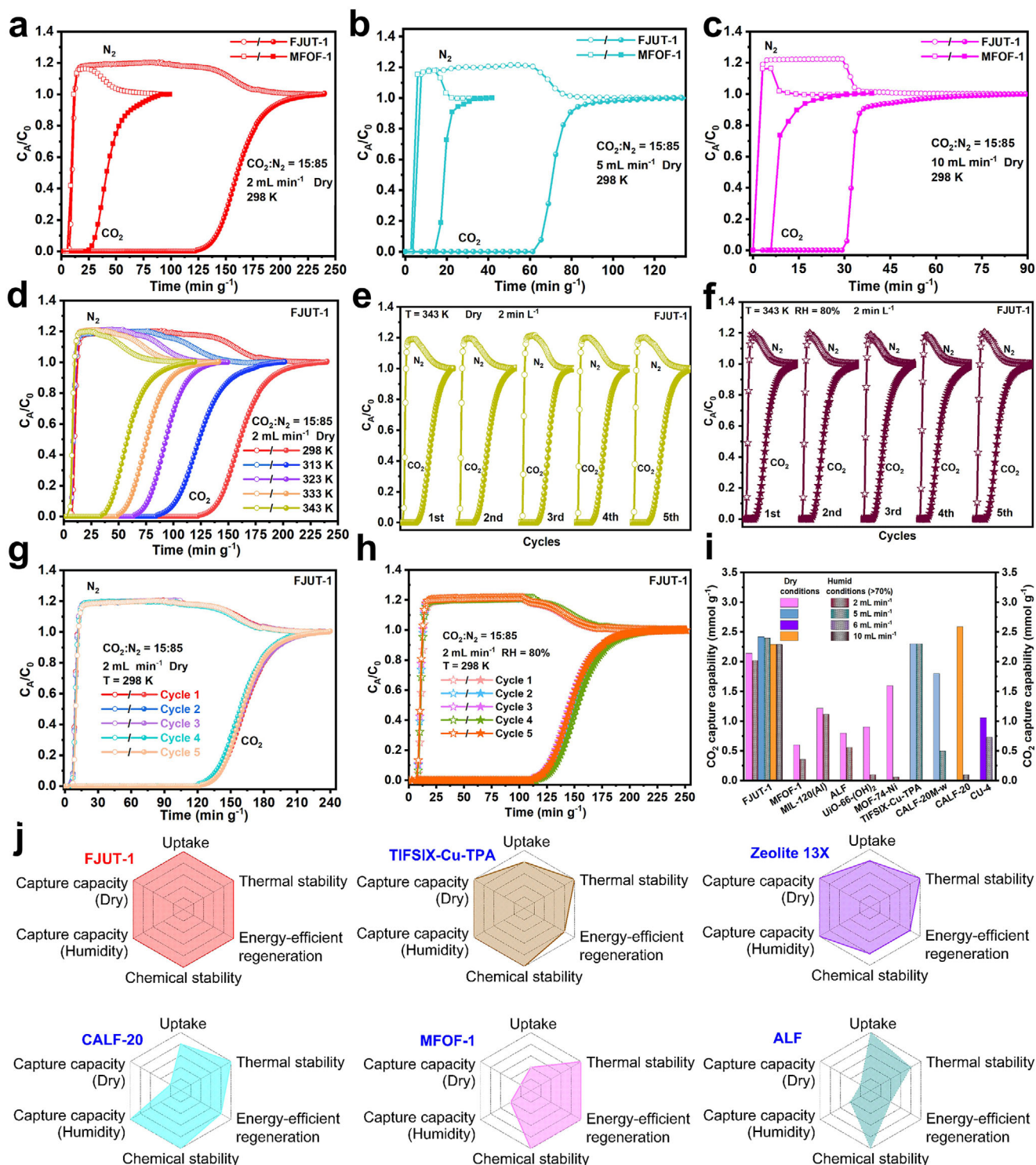


**Figure 3.** Experimental column breakthrough curves of MFOF-1 and FJUT-1 for  $\text{CO}_2/\text{N}_2$  (15:85, dry) mixtures with a total flow of a)  $2 \text{ mL min}^{-1}$ , b)  $5 \text{ mL min}^{-1}$ , c)  $10 \text{ mL min}^{-1}$ , respectively, under ambient conditions. d) Breakthrough curves of FJUT-1 for  $\text{CO}_2/\text{N}_2$  (15:85, dry) with a total flow of  $2 \text{ mL min}^{-1}$  at 1 bar and various temperatures. Recyclability of FJUT-1 for  $\text{CO}_2/\text{N}_2$  (15:85) mixtures with a total flow of  $2 \text{ mL min}^{-1}$  in multiple breakthrough tests under e) dry and f) 80% humidity at 343 K and 1 bar. Cycling tests of  $\text{CO}_2/\text{N}_2$  (15:85) mixtures under g) dry and h) 80% humidity at 298 K and 1 bar. i) Comparison of the capture capacity of  $\text{CO}_2$  under dry and humid conditions from breakthrough experiments. j) The comprehensive comparison of uptake, capture capacity, stability, and regenerability for FJUT-1 and other benchmark materials.

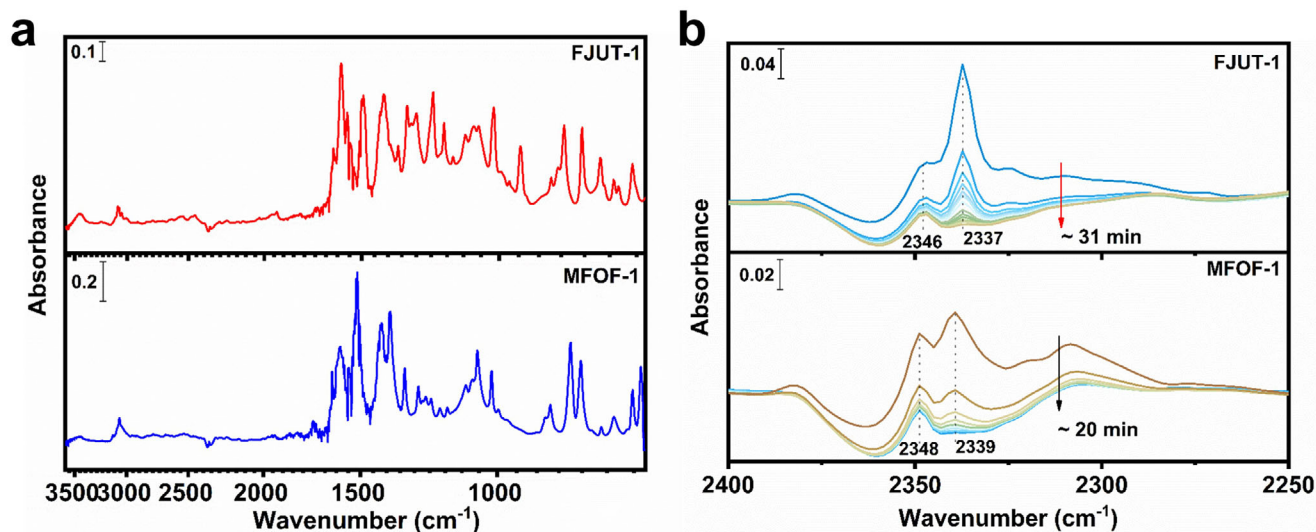


**Figure 4.** a) In situ FT-IR spectra of activated *proto*-MFOF-1 and FJUT-1, referenced to a pure KBr pellet in vacuum. b) Difference spectra showing the C–O stretching band of adsorbed CO<sub>2</sub> in *proto*-MFOF-1 (bottom) and FJUT-1 (top) samples upon loading at the pressure of 1 bar (top spectrum in each panel) and subsequent evacuation of the gas phase under vacuum for  $\approx 20$  and  $\approx 31$  mins, respectively. Each is referenced to the spectrum of activated sample.

vibrational bands associated with the tripodal carboxylic acid and pyridine linkers. Afterward, pure CO<sub>2</sub> was gradually purged into the chamber filled with *proto*-MFOF-1 or FJUT-1 samples until reaching the pressure of  $\approx 1$  bar, and held for  $\approx 10$  mins to ensure adsorption saturation. The desorption process was implemented via pumping the samples under high vacuum. As represented in Figure 4b, while the chamber was evacuated for  $\approx 10$  secs to remove the gas-phase CO<sub>2</sub> before recording the IR spectra, it seems difficult to remove the free CO<sub>2</sub> completely. The bands located at 2346 and 2348 cm<sup>-1</sup> for *proto*-MFOF-1 and FJUT-1 could be assigned to the C–O stretching bands of free CO<sub>2</sub> molecules. Compared with *proto*-MFOF-1 (2339 cm<sup>-1</sup>), a sharper and stronger band at  $\approx 2337$  cm<sup>-1</sup> is observed in FJUT-1, which represents the C–O stretching band of the incarcerated CO<sub>2</sub> within the confined cavity, demonstrating stronger framework-CO<sub>2</sub> interactions in FJUT-1. Moreover, the intensity of C–O stretching band in FJUT-1 gradually decreases along with the increasing desorption time, and disappears completely until  $\approx 31$  mins, while that in *proto*-MFOF-1 disappears completely after only  $\approx 20$  mins, further confirming the enhanced framework-CO<sub>2</sub> interactions in FJUT-1. Noteworthy, the 2337 cm<sup>-1</sup> band experiences a red-shift of 12 cm<sup>-1</sup> with respect to the gas-phase CO<sub>2</sub> ( $\approx 2349$  cm<sup>-1</sup>), implying host-guest interactions occur involving O...C–O forces and multiple HBs as evidenced by in situ SCXRD results, which weakens the C–O bonds, thus leading to the decrease of C–O stretching frequencies.

## 2.6. In Situ Single-Crystal X-Ray Diffraction (SCXRD) Studies

To probe the CO<sub>2</sub> adsorption mechanism on FJUT-1, the in situ CO<sub>2</sub> loading SCXRD experiments on FJUT-1 were performed, in which the activated FJUT-1 crystal was exposed to a CO<sub>2</sub> atmosphere for 1 h at room temperature. SCXRD analysis reveals that approximately twelve CO<sub>2</sub> molecules are captured in a unit

cell of FJUT-1, wherein the CO<sub>2</sub> molecules are mainly located in the T<sub>c</sub>-B cage decorated with electronegative F<sup>-</sup> and SO<sub>4</sub><sup>2-</sup> anions, and accessible pyridine/benzene rings (Figure 5a; Figure S62 and Table S1, Supporting Information). The CO<sub>2</sub> molecules in T<sub>c</sub>-B cage of FJUT-1 are trapped by O...C=O electrostatic interaction (2.91 Å) from one SO<sub>4</sub><sup>2-</sup> anion and C=O...H HBs interactions (distances range from 2.71 to 3.58 Å) from one pyridine ring and one benzene ring (Figure 5a). Additionally, obvious adsorbate-adsorbate interactions in the T<sub>c</sub>-B cage are observed with the O...C=O distance of 3.95 Å, probably due to the enhanced confinement effect in FJUT-1 (Figure 5b). The distinct host-guest and guest-guest interactions that existed in FJUT-1 collaboratively promote the selective CO<sub>2</sub> adsorption. On the contrary, almost no CO<sub>2</sub> molecules can be observed in the cages of *proto*-MFOF-1, implying the enhanced CO<sub>2</sub> capture potential for FJUT-1. These results reveal the efficiency of the CPSE strategy to facilitate post-combustion capture of CO<sub>2</sub> through optimizing the pore nanospace of cage-like mixed-ligand MOFs.

## 2.7. Molecular Simulations

To gain further insight into the selective adsorption mechanism, DFT calculations were implemented. Figure 6a,b; Figure S63 (Supporting Information) show the preferential CO<sub>2</sub> and N<sub>2</sub> binding sites in *proto*-MFOF-1 and FJUT-1, wherein CO<sub>2</sub> and N<sub>2</sub> are mainly incarcerated in the tetrahedral T<sub>c</sub>-B cage. Specifically, for *proto*-MFOF-1, CO<sub>2</sub> is banded in the corner of T<sub>c</sub>-B cage composed of one TPT linker, one BTB linker, and one Co<sub>4</sub> cluster, wherein the electrostatic O...C=O interactions (2.98 and 3.10 Å) and multiple C–O...H HBs (2.57, 2.61, 2.84, and 3.52 Å) happen. No obvious CO<sub>2</sub>-CO<sub>2</sub> interactions can be observed in *proto*-MFOF-1 (Figure 6c). In comparison, N<sub>2</sub> interacts with the framework mainly through C–H...N HBs with the distances ranging from 2.85 to 3.06 Å (Figure S63a, Supporting

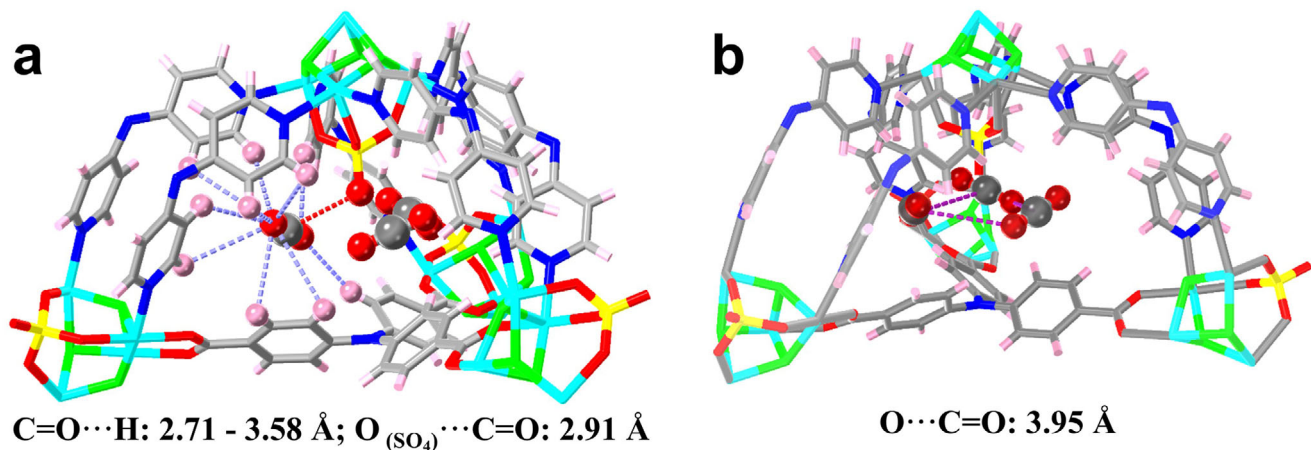


**Figure 5.** a) The CO<sub>2</sub> binding sites in gas-loaded FJUT-1 determined by SCXRD analysis. b) Dense packing of CO<sub>2</sub> molecules distribution in the Tc-B cage within FJUT-1.

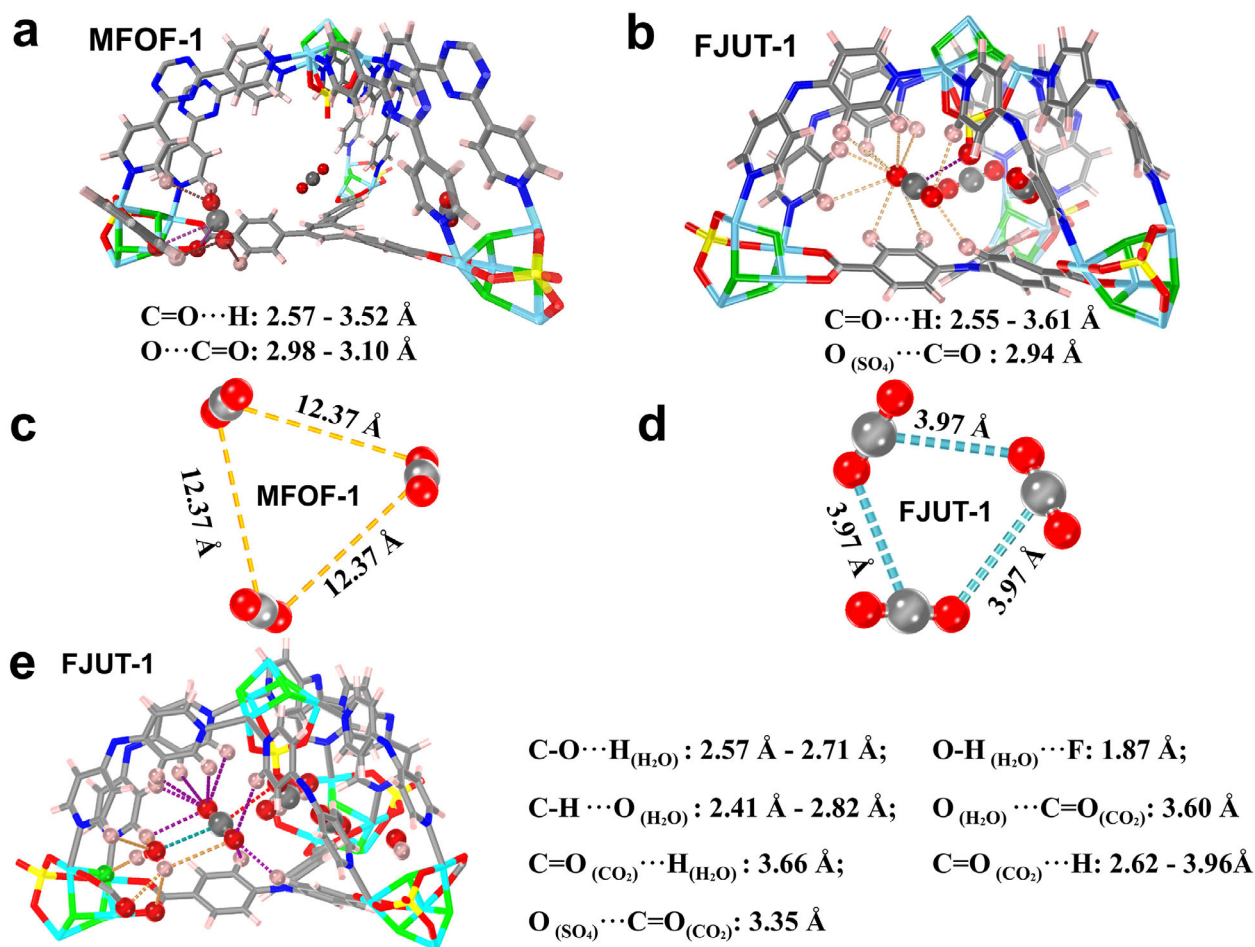


**Figure 6.** DFT calculated preferential adsorption sites of a) CO<sub>2</sub> in MFOF-1 and b) CO<sub>2</sub> in FJUT-1.<sup>[40]</sup> Packing mode of c) CO<sub>2</sub>-loaded MFOF-1 and d) CO<sub>2</sub>-loaded FJUT-1. e) Binding sites of CO<sub>2</sub> with H<sub>2</sub>O in FJUT-1.

Information). For FJUT-1, CO<sub>2</sub> is fixed in the similar corner of T<sub>c</sub>-B cage as that in *proto*-MFOF-1, yet stronger framework-CO<sub>2</sub> interactions involving electrostatic O...C=O interactions (2.94 Å) and multiple C—O...H HBs (2.55, 2.57, 2.68, 2.97, 3.21, 3.28, 3.37, 3.54, and 3.61 Å), consistent with the in situ SCXRD results, suggesting enhanced CO<sub>2</sub> capture capacity in FJUT-1 (Figure 6b, Table S4, Supporting Information). Additionally, guest-guest interactions are observed in FJUT-1 with the electrostatic C—O...C distance of 3.97 Å (Figure 6d). For comparison, N<sub>2</sub> is located in the T<sub>c</sub>-B cage through C—H...N HBs with the distances ranging from 2.74 to 3.01 Å (Figure S63b, Supporting Information). The shorter interactions distances and more action sites for CO<sub>2</sub> whether in *proto*-MFOF-1 or FJUT-1 indicate stronger CO<sub>2</sub> affinity than that of N<sub>2</sub>. The calculated CO<sub>2</sub> (20.4 kJ mol<sup>-1</sup>) and N<sub>2</sub> (11.3 kJ mol<sup>-1</sup>) binding energies for FJUT-1 are higher than those in *proto*-MFOF-1 (CO<sub>2</sub>: 12.6, N<sub>2</sub>: 6.6 kJ mol<sup>-1</sup>), manifesting strengthened framework-gas interactions and improved CO<sub>2</sub>/N<sub>2</sub> separation performance in FJUT-1 attributed to the enhanced cage confinement effect. To probe the effect of water on CO<sub>2</sub> adsorption, the simulation for H<sub>2</sub>O and CO<sub>2</sub> co-adsorption was executed. As shown in Figure 6e; Table S4 (Supporting Information) H<sub>2</sub>O is preferentially trapped in the corner of T<sub>c</sub>-B cage through O—H...F (1.87 Å), C—H...O (2.41 and 2.82 Å), and C—O...H (2.57 and 2.71 Å) HBs. While H<sub>2</sub>O occupies a few binding sites, it also provides extra adsorption sites for CO<sub>2</sub> via electrostatic O...C=O interaction (3.60 Å), and C—O...H HB (3.66 Å). Importantly, the electrostatic O...C=O (3.35 Å) interaction between the oxygen atom from SO<sub>4</sub><sup>2-</sup> anion and carbon atom from CO<sub>2</sub> remains intact after H<sub>2</sub>O introduction. This forms a strong CO<sub>2</sub>-nanotrap, promoting CO<sub>2</sub> capture, which agrees well with the breakthrough experiment under 60% humidity (Figure S53, Supporting Information). In addition to this, similar C—H...O HBs interactions (2.62, 2.67, 2.71, 3.14, 3.21, 3.36, 3.51, and 3.96 Å) as that observed amid dry conditions are observed. The calculated CO<sub>2</sub> binding energy in CO<sub>2</sub>/H<sub>2</sub>O co-adsorbed FJUT-1 is 37.4 kJ mol<sup>-1</sup>, much higher than that in CO<sub>2</sub> adsorbed FJUT-1, which turns out that the existence of H<sub>2</sub>O promotes the CO<sub>2</sub> adsorption to a certain degree, thus resulting in most of the CO<sub>2</sub> capture capacity for FJUT-1 under humid conditions being preserved. Overall, the reduced cage window size, preserved cage volume, combined with the functionalized cage surface in FJUT-1 collaboratively contribute to the significantly improved CO<sub>2</sub> capture capacity in comparison with *proto*-MFOF-1.

### 3. Conclusion

In summary, we have developed a facile CPSE strategy to construct cage-like mixed-ligand MOF, FJUT-1, with optimized pore nanospace, via IRC approach, for highly efficient CO<sub>2</sub> capture from wet-hot flue gas. Owing to the high connectivity of Co<sub>4</sub> cluster and strong Co-N/O coordination bonds, as well as the lower energy state induced by boiling acidic solution during the structure formation, FJUT-1 presents excellent physicochemical stability. Compared with *proto*-MFOF-1, FJUT-1 showcases significantly improved CO<sub>2</sub> adsorption capacity and selective CO<sub>2</sub> separation performance, ascribed to the reduced cage window size, preserved cage volume, and functionalized cage surface being adorned by F<sup>-</sup> anions, SO<sub>4</sub><sup>2-</sup> anions, and accessible pyridine/benzene rings. Furthermore, the moderate adsorption en-

thalpy enables FJUT-1 to regenerate easily with a low energy penalty. Together with the robust framework stability, FJUT-1 can be utilized to the consecutive CO<sub>2</sub> capture processes from wet-hot flue gas with high CO<sub>2</sub> capture capacity, corroborated by dynamic breakthrough experiments under high humidity and temperature. Comprehensive experiments involving in situ SCXRD and in situ FT-IR, combined with molecular modeling, reveal that FJUT-1 showcases dramatically enhanced affinity toward CO<sub>2</sub> than *proto*-MFOF-1 as a consequence of the strengthened cage confinement effect via stronger electrostatic O...C=O, multiple C—H...O, and guest-guest interactions. This work demonstrates the effectiveness of the CPSE approach for optimizing the pore nanospace of cage-like mixed-ligand MOFs for enhanced CO<sub>2</sub> capture applications in hot-wet flue gas, thus prompting the future design and construction of novel cage-like MOFs for practical separation applications.

### Supporting Information

Supporting Information is available from the Wiley Online Library or from the author.

### Acknowledgements

The authors acknowledge the financial support from National Natural Science Foundation of China (21701024, 22471294, and 22001271), Major International Science and Technology Cooperation Projects of Fujian Province (202510053), Collaborative Innovation Platform in the National Independent Innovation Demonstration Zone of Fuzhou-Xiamen-Quanzhou of China (2023-P-007), Scientific Research Foundation of Xiamen University of Technology (YKJ25007R), and Guangdong Introducing Innovative and Entrepreneurial Teams (2023ZT10L061). Partial support from the Robert A. Welch Foundation (B-0027) (SM) and the Ongoing Research Funding Program (ORF-2025-79), King Saud University, Riyadh, Saudi Arabia (AN) is also acknowledged.

### Conflict of Interest

The authors declare no conflict of interest.

### Data Availability Statement

The data that support the findings of this study are available from the corresponding author upon reasonable request.

### Keywords

CO<sub>2</sub> capture, coordination pore-space engineering, isorecticular contraction, metal-organic frameworks

Received: September 17, 2025  
Revised: October 29, 2025  
Published online: November 18, 2025

- [1] J. Rogel, O. Fricko, M. Meinshausen, V. Krey, J. J. Zilliacus, K. Riahi, *Nat. Commun.* **2017**, *8*, 15748.

- [2] R. Sahoo, S. Mondal, D. Mukherjee, M. C. Das, *Adv. Funct. Mater.* **2022**, *32*, 2207197.
- [3] G. T. Rochelle, *Science* **2009**, *325*, 1652.
- [4] J. Du, W. Yang, L. Xu, L. Bei, S. Lei, W. Li, H. Liu, B. Wang, L. Sun, *Chem. Eng. J.* **2024**, *488*, 150954.
- [5] M. Khraisheh, S. Mukherjee, A. Kumar, F. Al Momani, G. Walker, M. J. Zaworotko, *J. Environ. Manage.* **2020**, *255*, 109874.
- [6] J. H. Yan, M. M. Wu, Y. W. Sun, T. T. Ji, K. P. Yu, W. W. Dong, Y. Liu, Y. L. Gao, B. B. Sun, G. H. He, Y. Liu, *Adv. Funct. Mater.* **2025**, *35*, 2506327.
- [7] K. Sumida, D. L. Rogow, J. A. Mason, T. M. McDonald, E. D. Bloch, Z. R. Herm, T.-H. Bae, J. R. Long, *Chem. Rev.* **2012**, *112*, 724.
- [8] M. Usman, N. Iqbal, T. Noor, N. Zaman, A. Asghar, M. M. Abdelnaby, A. Galadima, A. Helal, *Chem. Rec.* **2021**, *22*, 202100230.
- [9] J. Y. Ren, D. Zhao, *Adv. Funct. Mater.* **2023**, *34*, 2307778.
- [10] W. T. Jiang, C.-C. Liang, Y.-B. Zhang, *Adv. Funct. Mater.* **2024**, *34*, 2308946.
- [11] Z.-M. Ye, Y. Xie, K. O. Kirlikovali, S. C. Xiang, O. K. Farha, B. L. Chen, *J. Am. Chem. Soc.* **2025**, *147*, 5495.
- [12] R. A. Maia, B. Louis, W. L. Gao, Q. Wang, *React. Chem. Eng.* **2021**, *6*, 1118.
- [13] H. Q. Pan, C. Yu, X. Suo, L. F. Yang, X. L. Cui, H. B. Xing, *Mater. Chem. Front.* **2023**, *7*, 6463.
- [14] S. Bose, D. Sengupta, T. M. Rayder, X. L. Wang, K. O. Kirlikovali, A. K. Sekizkardes, T. Islamoglu, O. K. Farha, *Adv. Funct. Mater.* **2023**, *34*, 2307478.
- [15] W. L. Li, Q. Shuai, J. M. Yu, *Small* **2024**, *20*, 2402783.
- [16] A. Kumar, D. G. Madden, M. Lusi, K.-J. Chen, E. A. Daniels, T. Curtin, J. J. Perry IV, M. J. Zaworotko, *Angew. Chem., Int. Ed.* **2015**, *54*, 14372.
- [17] A. Justin, J. Espín, M. J. Pougin, D. Stoian, T. Schertenleib, M. Mensi, I. Kochetygov, A. Ortega-Guerrero, W. L. Queen, *Adv. Funct. Mater.* **2023**, *34*, 2307430.
- [18] G. Y. Zhang, F. Xie, S. Ullah, L. L. Ma, S. J. Teat, S. Q. Ma, T. Thonhauser, K. Tan, H. Wang, J. Li, *J. Mater. Chem. A* **2024**, *12*, 32385.
- [19] L. Jiang, J. Y. Yong, R. Y. Xie, P. F. Xie, X. J. Zhang, Z. J. Chen, Z. B. Bao, *SusMat* **2023**, *3*, 609.
- [20] A. Rajendran, G. K. H. Shimizu, T. K. Woo, *Adv. Mater.* **2024**, *36*, 2301730.
- [21] K. Klemenčič, A. Krajnc, A. Puškarič, M. Huš, D. Marinič, B. Likozar, N. Z. Logar, M. Mazaj, *Angew. Chem., Int. Ed.* **2025**, *64*, 202424747.
- [22] P. M. Bhatt, Y. Belmabkhout, A. Cadiou, K. Adil, O. Shekhah, A. Shkurenko, L. J. Barbour, M. Eddaoudi, *J. Am. Chem. Soc.* **2016**, *138*, 9301.
- [23] H. A. Evans, D. Mullangi, Z. Y. Deng, Y. X. Wang, S. B. Peh, F. X. Wei, J. Wang, C. M. Brown, D. Zhao, P. Canepa, A. K. Cheetham, *Sci. Adv.* **2022**, *8*, ade1473.
- [24] Z. Q. Zhang, Z. Y. Deng, H. A. Evans, D. Mullangi, C. J. Kang, S. B. Peh, Y. X. Wang, C. M. Brown, J. Wang, P. Canepa, A. K. Cheetham, D. Zhao, *J. Am. Chem. Soc.* **2023**, *145*, 11643.
- [25] Z. Q. Zhang, D. Zhao, *Chem. Bio. Eng.* **2024**, *1*, 366.
- [26] X. Chen, D. Menon, X. L. Wang, M. He, M. R. A. Kiapi, M. Asgari, Y. X. Lyu, X. H. Tang, L. L. Keenan, W. Shepard, L. H. Wee, S. H. Yang, O. K. Farha, D. Fairen-Jimenez, *Chem* **2025**, *11*, 102382.
- [27] J. Y. Pei, H. M. Wen, X. W. Gu, Q. L. Qian, Y. Yang, Y. J. Cui, B. Li, B. L. Chen, G. D. Qian, *Angew. Chem., Int. Ed.* **2021**, *60*, 25068.
- [28] X. Zhang, R.-B. Lin, H. Wu, Y. H. Huang, Y. X. Ye, J. G. Duan, W. Zhou, J.-R. Li, B. L. Chen, *Chem. Eng. J.* **2022**, *431*, 134184.
- [29] Z. Q. Zhang, Y. L. Chen, K. G. Chai, C. J. Kang, S. B. Peh, H. Li, J. Y. Ren, X. S. Shi, X. Han, C. Dejoie, S. J. Day, S. H. Yang, D. Zhao, *Nat. Commun.* **2023**, *14*, 3789.
- [30] R. P. Loughran, T. Hurley, A. Gładysiak, A. Chidambaram, K. Khivantsev, E. D. Walter, T. R. Graham, P. Reardon, J. Szanyi, D. B. Fast, Q. R. S. Miller, A.-H. A. Park, K. C. Stylianou, *Cell Rep. Phys. Sci.* **2023**, *4*, 101470.
- [31] D. H. Song, F. L. Jiang, D. Q. Yuan, Q. H. Chen, M. C. Hong, *Small* **2023**, *19*, 2302677.
- [32] L. Zhang, Z. Y. He, Y. P. Liu, J. J. You, L. H. Lin, J. H. Jia, S. Chen, N. B. Hua, L.-A. Ma, X. Y. Ye, Y. R. Liu, C.-X. Chen, Q. T. Wang, *ACS Appl. Mater. Interfaces* **2023**, *15*, 30394.
- [33] H. Li, C. P. Liu, C. Chen, Z. Y. Di, D. Q. Yuan, J. D. Pang, W. Wei, M. Y. Wu, M. C. Hong, *Angew. Chem., Int. Ed.* **2021**, *60*, 7547.
- [34] S.-Y. Li, S.-C. Fan, P. Zhang, W.-Y. Yuan, Y. Wang, Q.-G. Zhai, *Chem* **2024**, *10*, 2761.
- [35] Y.-Z. Hao, K. Shao, X. Zhang, Y.-H. Yu, D. Liu, H.-M. Wen, Y. J. Cui, B. Li, B. L. Chen, G. D. Qian, *J. Am. Chem. Soc.* **2025**, *147*, 11257.
- [36] Y. Q. Hu, Y. J. Jiang, J. H. Li, L. Y. Wang, M. Steiner, R. F. Neumann, B. Q. Luan, Y. B. Zhang, *Adv. Funct. Mater.* **2023**, *33*, 2213915.
- [37] Q.-G. Zhai, X. H. Bu, X. Zhao, D.-S. Li, P. Y. Feng, *Acc. Chem. Res.* **2017**, *50*, 407.
- [38] W. Wang, Y. C. Chen, P. Y. Feng, X. H. Bu, *Adv. Mater.* **2024**, *36*, 2403834.
- [39] Y. C. Xiao, Y. C. Chen, W. Wang, X. H. Bu, P. Y. Feng, *Angew. Chem., Int. Ed.* **2024**, *63*, 202403698.
- [40] L. Zhang, T. T. Xiao, X. Y. Zeng, J. J. You, Z. Y. He, C.-X. Chen, Q. T. Wang, A. Nafady, A. M. Al-Enizi, S. Q. Ma, *J. Am. Chem. Soc.* **2024**, *146*, 7341.
- [41] L. Zhang, W. B. Yang, X. Y. Wu, C. Z. Lu, W. Z. Chen, *Chem. - Eur. J.* **2016**, *22*, 11283.
- [42] Z. Liu, C. Shen, F. V. S. Lopes, P. Li, J. Yu, C. A. Grande, A. E. Rodrigues, *Sep. Sci. Technol.* **2013**, *48*, 38.
- [43] W. B. Liang, P. M. Bhatt, A. Shkurenko, K. Adil, G. Mouchaham, H. Aggarwal, A. Mallick, A. Jamal, Y. Belmabkhout, M. Eddaoudi, *Chem* **2019**, *5*, 950.
- [44] Y. Zhou, J. L. Zhang, L. Wang, X. L. Cui, X. L. Liu, S. S. Wong, H. An, N. Yan, J. Y. Xie, C. Yu, P. X. Zhang, Y. H. Du, S. B. Xi, L. R. Zheng, X. Z. Cao, Y. J. Wu, Y. X. Wang, C. Q. Wang, H. M. Wen, L. Chen, H. B. Xing, J. Wang, *Science* **2021**, *373*, 315.
- [45] J. B. Lin, T. T. T. Nguyen, R. Vaidhyanathan, J. Burner, J. M. Taylor, H. Durekova, F. Akhtar, R. K. Mah, O. Ghaffari-Nik, S. Marx, N. Fylstra, S. S. Iremonger, K. W. Dawson, P. Sarkar, P. Hovington, A. Rajendran, T. K. Woo, G. K. H. Shimizu, *Science* **2021**, *374*, 1464.
- [46] C.-X. Chen, T. Pham, K. Tan, R. Krishna, P. C. Lan, L. F. Wang, S. B. Chen, A. M. Al-Enizi, A. Nafady, K. A. Forrest, H. P. Wang, S. C. Wang, C. Shan, L. Zhang, C.-Y. Su, S. Q. Ma, *Cell Rep. Phys. Sci.* **2022**, *3*, 100977.
- [47] Q. B. Dong, J. M. Wan, H. H. Chen, Y. H. Huang, J. G. Duan, *ACS Appl. Mater. Interfaces* **2023**, *15*, 39606.
- [48] X. X. Wang, M. Alzayer, A. J. Shih, S. Bose, H. M. Xie, S. M. Vornholt, C. D. Malliakas, H. Alhashem, F. Joodaki, S. Marzouk, G. Xiong, M. Del Campo, P. Le Magueres, F. Formalik, D. Sengupta, K. B. Idrees, K. Ma, Y. W. Chen, K. O. Kirlikovali, T. Islamoglu, K. W. Chapman, R. Q. Snurr, O. K. Farha, *J. Am. Chem. Soc.* **2024**, *146*, 3943.
- [49] Z.-G. Hu, Y.-X. Wang, S. Farooq, D. Zhao, *AIChE J.* **2017**, *63*, 4103.
- [50] T. Li, D.-L. Chen, J. E. Sullivan, M. T. Kozlowski, J. K. Johnson, N. L. Rosti, *Chem. Sci.* **2013**, *4*, 1746.
- [51] T. M. McDonald, D. M. D'Alessandro, R. Krishna, J. R. Long, *Chem. Sci.* **2011**, *2*, 2022.
- [52] J. H. Choe, H. Kim, M. J. Kang, H. Yun, S. Y. Kim, S. M. Lee, C. S. Hong, *J. Am. Chem. Soc.* **2022**, *144*, 10309.
- [53] T. M. McDonald, W. R. Lee, J. A. Mason, B. M. Wiers, C. S. Hong, J. R. Long, *J. Am. Chem. Soc.* **2012**, *134*, 7056.
- [54] L. Y. Li, J. W. Wang, Z. G. Zhang, Q. W. Yang, Y. W. Yang, B. G. Su, Z. B. Bao, Q. L. Ren, *ACS Appl. Mater. Interfaces* **2018**, *11*, 2543.
- [55] R. A. Smaldone, R. S. Forgan, H. Furukawa, J. J. Gassensmith, A. M. Z. Slawin, O. M. Yaghi, J. F. Stoddart, *Angew. Chem., Int. Ed.* **2010**, *49*, 8630.

- [56] H. Lyu, O. I.-F. Chen, N. Hanikel, M. I. Hossain, R. W. Flaig, X. K. Pei, A. Amin, M. D. Doherty, R. K. Impastato, T. G. Glover, D. R. Moore, O. M. Yaghi, *J. Am. Chem. Soc.* **2022**, *144*, 2387.
- [57] H.-M. Wen, C. J. Liao, L. B. Li, A. Alsalmeh, Z. Allothman, R. Krishna, H. Wu, W. Zhou, J. Hu, B. L. Chen, *J. Mater. Chem. A* **2019**, *7*, 3128.
- [58] Y. L. Peng, T. Pham, P. F. Li, T. Wang, Y. Chen, K. J. Chen, K. A. Forrest, B. Space, P. Cheng, M. J. Zaworotko, Z. J. Zhang, *Angew. Chem., Int. Ed.* **2018**, *57*, 10971.
- [59] O. Shekhah, Y. Belmabkhout, Z. J. Chen, V. Guillerm, A. Cairns, K. Adil, M. Eddaoudi, *Nat. Commun.* **2014**, *5*, 4228.
- [60] B. L. Chen, D. Fan, R. V. Pinto, I. Dovgaliuk, S. Nandi, D. Chakraborty, N. García-Moncada, A. Vimont, C. J. McMonagle, M. Bordinhos, A. Al Mohtar, I. Cornu, P. Florian, N. Heymans, M. Daturi, G. De Weireld, M. Pinto, F. Nouar, G. Maurin, G. Mouchaham, C. Serre, *Adv. Sci.* **2024**, *11*, 2401070.